Received: 15 March 2022 | Revised: 20 April 2022 | Accepted: 20 April 2022
DOI: 10.37917/ijeee.18.1.13 Vol. 18| Issue 1| June 2022

Open Access

Iraqi Journal for Electrical and Electronic Engineering
Original Article

Grid-Forming and Grid-Following Based Microgrid Inverters Control

Ali M. Jasim*, Basil H. Jasim
Electrical Engineering Department, University of Basrah, Basrah, Iraq

Correspondence
*Ali M. Jasim
Electrical Engineering Department,
University of Basrah, Basrah, Iraq
Email: e.alim.j.92@gmail.com

Abstract
Microgrids (𝓜-grids) can be thought of as a small-scale electrical network comprised of a mix of Distributed Generation (DG) resources, storage devices, and a variety of load species. It provides communities with a stable, secure, and renewable energy supply in either off-grid (grid-forming) or on-grid (grid-following) mode. In this work, a control strategy of coordinated power management for a Low Voltage (LV) 𝓜-grid with integration of solar Photovoltaic (PV), Battery Energy Storage System (BESS) and three phase loads operated autonomously or connected to the utility grid has been created and analyzed in the Matlab Simulink environment. The main goal expressed here is to achieve the following points: (i) grid following, grid forming modes, and resynchronization mode between them, (ii) Maximum Power Point Tracking (MPPT) from solar PV using fuzzy logic technique, and active power regulator based boost converter using a Proportional Integral (PI) controller is activated when a curtailment operation is required, (iii) 𝓜-grid imbalance compensation (negative sequence) due to large single-phase load is activated, and (iv) detection and diagnosis the fault types using Discrete Wavelet Transform (DWT). Under the influence of irradiance fluctuation on solar plant, the proposed control technique demonstrates how the adopted system works in grid-following mode (PQ control), grid- formation, and grid resynchronization to seamlessly connect the 𝓜-grid with the main distribution system. In this system, a power curtailment management system is introduced in the event of a significant reduction in load, allowing the control strategy to be switched from MPPT to PQ control, permitting the BESS to absorb excess power. Also, in grid-following mode, the BESS's imbalance compensation mechanism helps to reduce the negative sequence voltage that occurs at the Point of Common Coupling (PCC) bus as a result of an imbalance in the grid's power supply. In addition to the features described above, this system made use of DWT to detect and diagnose various fault conditions.

KEYWORDS: Microgrid, Grid- Forming Grid- Support Inverter, Distributed Generation, PQ control, Droop Control, Wavelet Transform, Maximum Power Point tracking.

I. INTRODUCTION

Future power distribution systems are predicted to be more dependable, versatile, and intelligent than those now in use. The 𝓜-grid idea has been offered as a possible method to meet these goals [1]. With the help of power electronic devices and renewable energy sources, the concept of 𝓜-grid was introduced. Distributed Generations (DGs) are energy sources that are used to support power. Diesel generators, solar cells, fuel cells, and wind turbines are common 𝓜-grid Renewable Energy Resourced (RERs). To establish 𝓜-grid connection, each RER is frequently paired with power electronic equipment to form DG unit. Through its quick control action, RER with inverter can reduce oscillation [2].

The functionalities of a 𝓜-grid system based on the static transfer switch position are grid-tied mode and autonomous (islanded) mode [3]. In the event of a power outage, the 𝓜-grid should be operated in islanded mode to meet the load requirement. It should also maintain the appropriate power quality, improve system stability and power supply availability [4][5]. When 𝓜-grid is connected to the utility grid, it acts as a regulated load or generator, eliminating the power quality and safety issues that come with DGs connected directly to the grid [5]. The utility grid can provide voltage and frequency level control in the 𝓜-grid while operating in on-grid mode. However, in off-grid mode, all DG resources should be accountable for power balance as well as voltage and frequency level regulation in the 𝓜-grid network via active coordinated power management and power sharing control mechanisms [6].

The management of 𝓜-grid and the usage of renewable energy sources (RESs) in power systems has gained a lot of attention in recent years as networks progress toward smart grid operation. This is due to their ability to function in either grid-connected or islanded mode and ensure vital loads are supplied with power without interruption in the event of a

disaster. This notion, however, comes with its own set of issues, such as quick and precise islanding detection, effective regulation of voltages and frequencies inside the M-grid, detecting loss of synchronization and addressing the overload problems.

Many studies have been conducted in this context by a lot of researchers to solve the concerns mentioned above, such as, Wang, J. et al. in 2018 [7] and Zacharia, L et al. in 2019 [8] developed $\mathscr{M}$-grid energy management systems to schedule the $\mathscr{M}$-grid operation in each time step. In 2020 [9], Xiaoling Xiong and Yuchen Yang, proposed photovoltaic based DC microgrid (PVDCM) system which consists of a solar power system, a battery connected to the common bus via a boost converter and a bidirectional buck/boost converter, respectively. While the photovoltaic (PV) panels may be operating in MPPT mode or constant voltage mode, electricity can flow bidirectionally between the battery and the load. In 2020 [10], K. Rajasekhara Reddy et al. introduced a full examination of the few variants of the grid connected PV inverter system, as well as its control technique for tracking maximum power and producing pulses to achieve the needed output power. In 2020 [11], Lucas O. Mogaka et al proposed a control method for an operation of $\mathscr{M}$-grid powered by RERs capable of operating in both grid connected and islanded modes. When the $\mathscr{M}$-grid is disconnected from the main grid, the RERs controller system detects an islanding condition and switches to a voltage control mode. The interface control is meant to give consistent active and reactive electricity to the grid in on grid mode. After adequate resynchronization, an islanding detection algorithm will put the inverter into voltage control mode without harming the important loads if the grid is unplugged. In 2020 [12], Bilal Naji Alhasnawi and Basil H. Jasim, employed a home energy management system that alternates between distributed energy and grid power sources. The home energy management system includes controllers for MPPT, battery charge and discharge, and an inverter for effective regulation between different sources based on load requirements and source availability at maximum PowerPoint. In addition, MPPT approach has been applied to the PV to collect the maximum power from the hybrid power system when climatic circumstances change. In 2020 [13], Bilal Naji Alhasnawi and Basil H. Jasim proposed distributed coordinated control for hybrid $\mathscr{M}$-grid, which might be used in both grid-connected and islanded modes with hybrid energy supplies and changing loads. The suggested system enables the coordinated operation of distributed energy resources to provide active power and extra service as needed. In addition, MPPT approach has been used on both solar stations and wind turbines. In 2020 [14], Bilal Naji Alhasnawi and Basil H , proposed an energy management system to satisfy the demand, a hybrid system with distribution electric grid, photovoltaic, and batteries was used as an energy source in the consumer's home. In 2021 [15], Heesang Ko et al presented a strategy for coordinating supervisory power. The primary goal is to limit the penetration of additional electricity from RERs into the grid, hence preventing curtailments. To make it practical, the suggested approach is used to create a grid-connected microgrid system that will only run in response to demand changes and virtual power plant (VPP) requests. In 2021 [16], K.Rayudu et al, presented a mathematical model of a $\mathscr{M}$-grid composed of a wind power generation and PV system that are integrated into the utility grid, and a PI Controller for controlling the transition from grid-connected mode to island mode, with each DG inverter set to constant current control mode to provide preset power to the main grid. In an islanding situation, each DG inverter is connected to voltage control mode when it disconnects from the main grid. In 2021 [17], Nihad Abdulkhudhur Jasim and Majli Nema Hawas proposed an isolated DC $\mathscr{M}$-grid, utilizing solar photovoltaic (PV) as the RER source to deliver power to resistive DC charges, as well as a hybrid energy storage system (HESS) for battery and supercapacitor. To test this suggested technique for managing the DC bus voltage, several situations of load and solar insolation fluctuation are simulated. When the output waveforms with and without HESS are examined, a favorable decrease in transient voltage is found if the HESS is used. In 2021 [18], Mehmet Emin Akdogan and Sara Ahmed developed a modified reverse droop management strategy in the Energy Storage System (ESS) to improve three-phase PCC voltage quality in multi-microgrids (MMG). In 2021 [19], Mathiesen, P. et al. developed a power balancing technique for optimizing distributed energy resource investments in the intra-hour fluctuation of solar and demand of a home $\mathscr{M}$-grid for building the $\mathscr{M}$-grid strategy. This strategy helps to limit the risks of intra-hour forecasting variations. In 2021 [20], Mwaka I. Juma et al. proposed thorough design of the freestanding DC microgrid, as well as the detailed design of the DC bus voltage controller, which is the MPPT-based PI control algorithm with DC bus voltage regulation. The Ziegler–Nichols approach was used to fine-tune.

The present research's contributions can be summarized in the following points:

- The dynamic operation of a $\mathscr{M}$-grid consisting of (PV, BESS, and loads) linked/unlinked to the utility grid is studied and simulated.
- Grid-following mode, PQ control, and irradiance fluctuation are studied.
- Grid-following, grid-forming procedure and a resynchronization between them are performed.
- Maximum power point tracking from solar PV has been achieved using Perturb and Observe (P & O) algorithm and fuzzy logic techniques.
- Grid-forming mode and solar plant curtailment have been carried out.
- Detection and diagnosis the faults types using the discrete wavelet transform are performed.
- PQ control and imbalance (negative sequence) correction are introduced as an ancillary services.

II. Proposed System Configuration

The adopted electrical energy network is depicted in Fig.1.

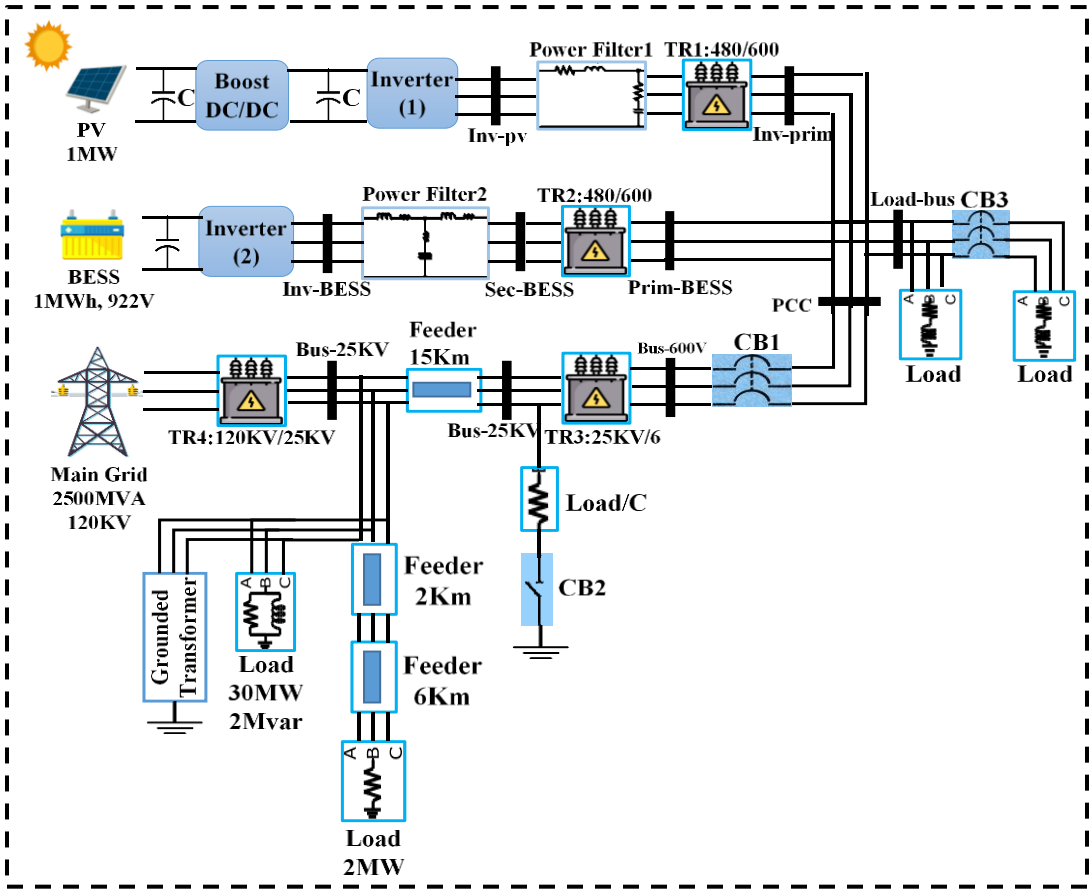

Fig. 1: The adopted electrical energy network

The proposed $\mathscr{M}$-grid is made up of the following major components: Distribution System, BESS, Solar PV and 600V Load.

1) Distribution System

A 120-kV grid equivalent, 25-kV feeders and transformers are used to represent the electrical grid. To link the microgrid to the distribution system, a three-phase breaker and a 25-kV/600V transformer are needed. In the grid branch, a single-phase load can be activated to cause a grid imbalance.

2) Solar Power Plant

Figure 2 depicts the equivalent circuit of a PV cell based on a single diode model, which can be represented as a diode, current source, series resistance, and parallel resistance.

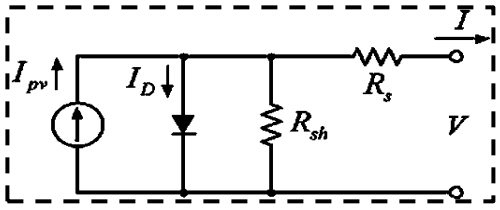

Fig. 2: Single diode based equivalent circuit of a PV cell

The I-V behavior of the circuit model comprised of one diode and two resistors is specified by the equation (1)[21].

$$I = I_{PV} - I_O\left\{\exp\left(\frac{V+IR_s}{\alpha V_T}\right) - 1\right\} - \frac{V+IR_s}{R_{sh}} \quad (1)$$

where I_{PV} is the photocurrent delivered by the constant current source; I_O is the diode's reverse saturation current; R_s is the series resistor that accounts for losses in cell solder bonds, interconnection, junction box, and so on; R_{sh} is the shunt resistor that accounts for current leakage through the high conductivity shunts across the p-n junction; and α is the ideality factor that accounts for the diodes' deviation from Shockley diffusion theory. V_T is not an unknown parameter; it is the diode's thermal voltage and is affected by the electron charge, q, the Boltzmann constant, k, the number of cells in series, n, and the temperature, T:

$$V_T = \mathrm{n}\frac{kT}{q} \quad (2)$$

The equivalent circuit parameters must be changed to match the behavior of the equivalent circuit of the solar cell/panel testing findings. This adjustment can be made numerically [22,23–28] or analytically [28–31]; based on empirically recorded I-V curves or just on data from the manufacturers' datasheets.

The solar plant comprises of a PV array capable of producing 1 MW at 1000 W/m2 of solar irradiance and a cell

temperature of 25 degrees Celsius. Figure 3 depicts the adopted PV array characteristics.

A boost converter is linked to the PV array and MPPT controller controls the boost. The MPP's exact position is uncertain, as it shifts with irradiance and temperature. As a result, the MPPT algorithms serve as guidelines for the MPPT controller to adjust the operating point toward the MPP in any circumstance. The P&O algorithm and fuzzy logic approaches have been used in this study. The MPPT use the Perturb and Observe approach to adjust the voltage across the PV array's terminals in order to collect the maximum amount of electricity. The MPPT controller perturbs the PV voltage by a little amount in this process, and the change in output power ΔP is then measured. If ΔP is positive, the operating point moves closer to the MPP, and the controller perturbs in the same direction again to move closer to that point (Case 1 in Fig. 4). If ΔP is negative, the operating point is distant from the MPP, and the controller reverses the direction of the perturbation as a result (Case 2 in Fig. 4). The process is continued until the MPP has been achieved.

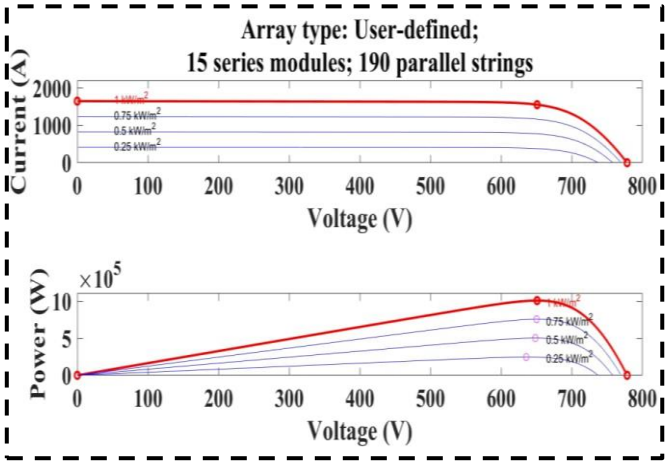

Fig. 3: The adopted PV array characteristics

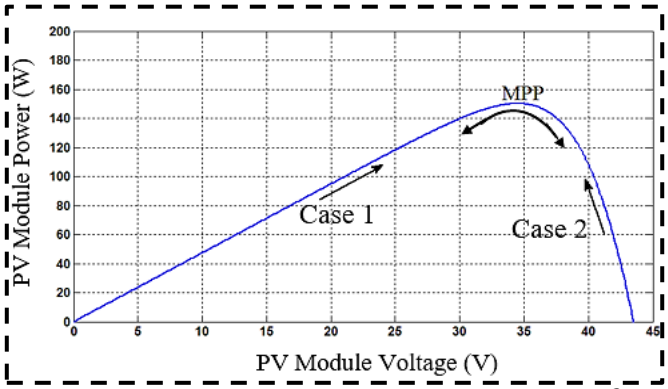

Fig.4. PV Module Power vs. Voltage at (G=1000W/m^2, T=25℃).

Although the P&O method is simple to develop, it has several flaws, including [32]:

- One of the significant disadvantages of the perturb and observe technique is that the output power oscillates around the maximum power point under steady state operation, resulting in fluctuating converter output.
- It can also track in the opposite direction, away from the MPP, when irradiance levels are quickly increasing or falling.

Fig.5 can be used to explain the second issue. Assume that the first state was at point A, with a 250 W/m2 irradiance level. If the irradiance level is suddenly increased to 500 W/m2 while the controller is in the process of dropping the voltage, the controller will continue to decrease the voltage, causing the MPP to mismatch and move toward point B. Any additional increase in irradiance causes the operational point to migrate away from MPP, toward points C and D, rather than toward points F, R, and H. If the controller was increasing the voltage action, the tracking would proceed toward points N, M, and O, causing the same issue. This means that during foggy days, the P&O algorithm fails at cloudy days.

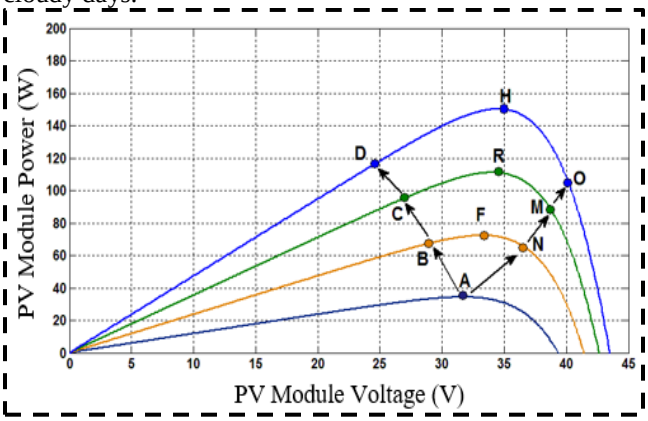

Fig.5 P&O algorithm error tracking under rapidly rising irradiance.

Working with imprecise inputs, not requiring a perfect mathematical model, and handling nonlinearity are all benefits of fuzzy logic controllers [33]. The three steps of fuzzy logic control are fuzzification, rule basis lookup table, and defuzzification. In the fuzzification step, membership functions based linguistic variables similar to that in Fig.6 can be obtained from numerical input variables. NB (negative large), NS (negative small), ZE (zero), PS (positive small), and PB (positive big) are the most commonly utilized membership functions [34]. The crisp values of the membership functions are represented by "a" and "b" in Fig.6.

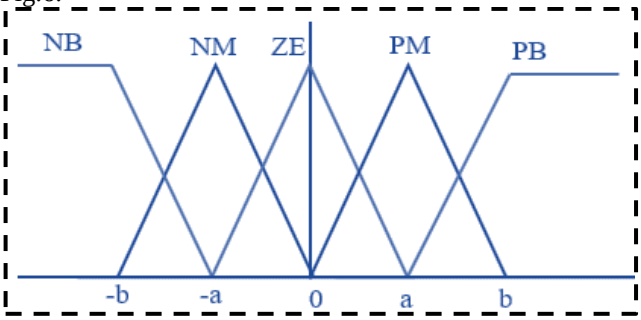

Fig.6: The fuzzy logic control's membership functions.

As inputs to the MPPT fuzzy logic controller, the error E(n)=ΔP/ΔV and the change in voltage ΔV (the user has the option to choose the inputs of this Controller) were utilized. Since dP/dV diminishes at MPP, then:

$$E(n) = \frac{P(n)-P(n-1)}{V(n)-V(n-1)} \quad (3)$$

$$\Delta V(n) = V(n) - V(n-1) \quad (4)$$

The fuzzy logic controller output, which is generally a change in duty ratio (ΔD) of the power converter, may be searched up in a rule base table if E and ΔV are computed and translated to linguistic variables. The linguistic variables (allocated to ΔD for various combinations of E and ΔV) are determined by the power converter in use as well as the user's understanding. The fuzzy logic controller output ΔD is changed from a linguistic variable to a numerical variable during the defuzzification stage [34].

Fuzzy logic-based MPPT controllers have proven to be effective in a variety of atmospheric circumstances. However, their success is heavily reliant on the user's or control engineer's ability to select the appropriate error computation and create the rule basis table. Whereas increasing the number of linguistic variables improves the output accuracy, it also increases the system's complexity. Fuzzy technique is used to obtain the MPP in this paper, and a Proportional Integral (PI) controller is adopted to control the boost when a curtailment operation is required.

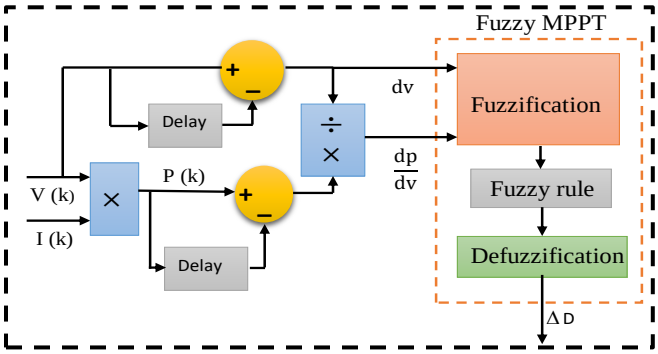

Fig.7: the fuzzy logic controller's block diagram

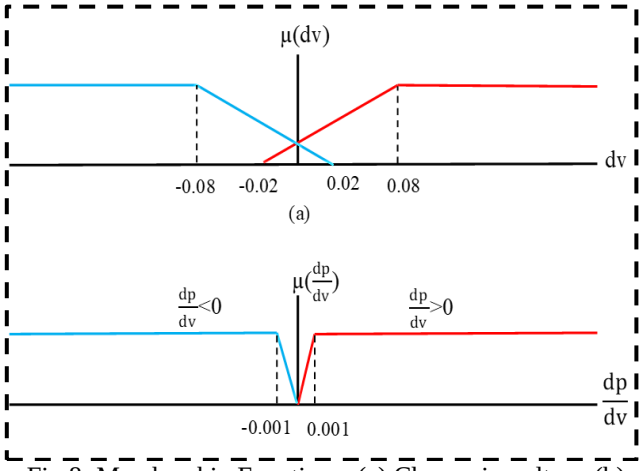

Fig.8: Membership Functions: (a) Change in voltage (b) Change in dp/dv

The fuzzy rules are written as:

- If dv is Neg. and dp/dv>0 then ΔD is 1
- If dv is Neg. and dp/dv<0 then ΔD is -0.2
- If dv is Pos. and dp/dv>0 then ΔD is 0.1
- If dv is Pos. and dp/dv<0 then ΔD is -0.8

The duty ratio change (ΔD) is added to the PWM generator's input, which consists of an integral and comparator with a saw tooth wave as a reference voltage.

The power declines over time, with the most power accessible at lower temperatures, as seen in (Beriber and Talha, 2013 [35]). Furthermore, according to (Younis et al. 2012 [36]), when a PV panel is directly connected to a load, the load impedance defines the PV module's operating state, and only the optimal load allows the PV module to collect the maximum power. Lodhi et al. 2017 [37] offered a comparison of the P&O approach with the Incremental Conductance (IC) method under stable and dynamic weather conditions. However, as compared to the P&O technique, IC hardware design is more difficult. While P&O systems are straightforward, the operating point oscillates about MPP, resulting in considerable power loss.

In current work, there are two operation modes of the boost converter to regulate the PV array: maximum power point tracking (MPPT) and curtailment. In mode 1, a fuzzy logic based MPPT algorithm calculates the boost converter duty cycle to ensure maximum power extraction from the array for a given solar irradiation. The duty cycle of the boost converter is adjusted to follow the active power reference in curtailment mode as shown in Fig.9.

The boost converters' output voltage (DC bus voltage) is 1000V. A three-level inverter (with a switching frequency of 2340 Hz) transforms the 1000 V DC to about 500 V AC. The inverter is regulated by a DC voltage regulator, whose function it is to keep the DC link voltage at 1000V no matter how much active power the PV arrays supply. To link the inverter to the microgrid, an LC power filter can be adopted in AC side and a 1-MVA 480V/600V three-phase coupling transformer is utilized (see Fig.1).

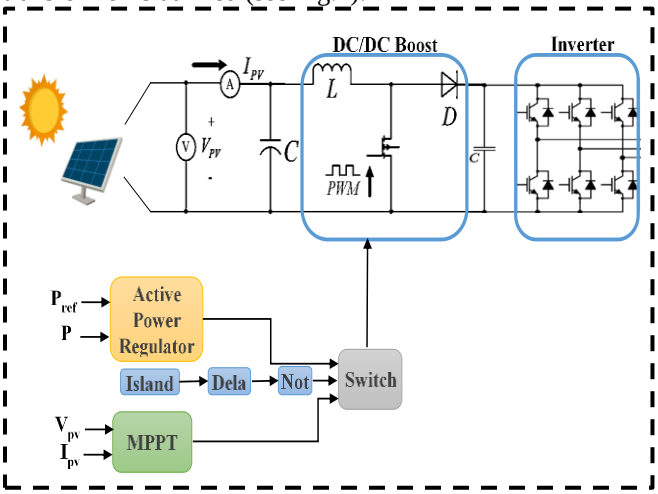

Fig.9 control method of PV-connected boost converter cascaded with inverter for MPPT and power curtailment modes.

For the typical three phase inverter model, the mathematical modeling of a three-phase grid-connected PV system is as follows.

$$\left.\begin{aligned} v_a &= R_f i_a + L_f \frac{di_a}{dt} + v_{ga} \\ v_b &= R_f i_b + L_f \frac{di_b}{dt} + v_{gb} \\ v_c &= R_f i_c + L_f \frac{di_c}{dt} + v_{gc} \end{aligned}\right\} \quad (5)$$

where v_a, v_b, v_c are the inverter side voltages, v_{ga}, v_{gb}, v_{gc} are the grid side voltages and i_a, i_b, i_c are the inverter output currents, R_f and L_f are the resistor and inductor of the LC power filter.

Equation (5) may be written as the current equation (6)

$$\left.\begin{aligned} \frac{di_a}{dt} &= -\frac{R_f}{L_f} i_a - \frac{1}{L_f} v_{ga} + \frac{1}{L_f} v_a \\ \frac{di_b}{dt} &= -\frac{R_f}{L_f} i_b - \frac{1}{L_f} v_{gb} + \frac{1}{L_f} v_b \\ \frac{di_c}{dt} &= -\frac{R_f}{L_f} i_c - \frac{1}{L_f} v_{gc} + \frac{1}{L_f} v_c \end{aligned}\right\} \quad (6)$$

The inverter control's primary function is to transmit the maximum amount of solar energy produced into the grid and to manage the dc-link voltage. As shown in Fig. 10, the suggested control strategy is based on two loops. The dc-link voltage is in the outer loop, while the inverter output current is in the inner loop. Around the inverter, three basic command blocks appear: the current loop, the dc-link voltage controller, and the phase-locked loop (PLL).

In electrical engineering, the αβ transformation or Clarke transformation is a mathematical transformation used to make three-phase circuit analysis easier. It's comparable to the dq0 transformation in terms of concept. One of the most useful applications of the αβ transformation is the generation of the reference signal required for space vector modulation control of three-phase inverters. Firstly, here the Clarke Transform block converts a three-phase current and voltage time-domain components in (abc) reference frame to components in a stationary (αβ) reference frame. The Clarke transform is implemented as follows:

$$\begin{bmatrix} \alpha \\ \beta \end{bmatrix} = \frac{2}{3} \begin{bmatrix} 1 & -0.5 & -0.5 \\ 0 & \frac{\sqrt{3}}{2} & -\frac{\sqrt{3}}{2} \end{bmatrix} \begin{bmatrix} a \\ b \\ c \end{bmatrix} \quad (7)$$

In the abc reference frame, the components of the three-phase system are a, b, and c. In the stationary reference frame, α and β are the components of the two-axis system.

The stationary reference frame of voltage signals are applied to PLL block to compute the phase difference angle. Then a transition of (αβ) Clarke components in a fixed reference frame to (dq) Park components in a rotating reference frame is performed by the (αβ) to dq block using equation (8).

$$\begin{bmatrix} d \\ q \end{bmatrix} = \begin{bmatrix} Cos\theta & Sin(\theta) \\ -Sin\theta & Cos(\theta) \end{bmatrix} \begin{bmatrix} \alpha \\ \beta \end{bmatrix} \quad (8)$$

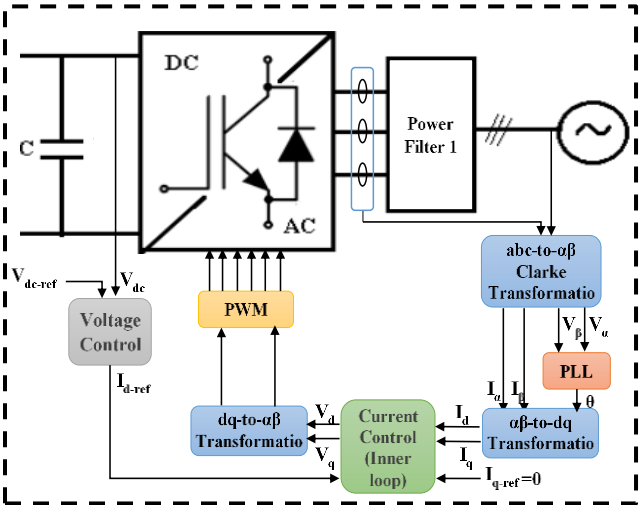

Fig.10 suggested control strategy of three phase PV inverter

The voltage control PI regulator is given by eqn. (9), and the current control PI regulators are given by eqns. (10) and (11).

$$I_{d-ref} = \left(k_{pvpv} + {k_{ivpv}}/{s}\right)\left(V_{dc-ref} - V_{dc}\right) \quad (9)$$

$$I_d = \left(k_{pipv} + {k_{iipv}}/{s}\right)\left(I_{d-ref} - I_d\right) \quad (10)$$

$$I_q = \left(k_{pipv} + {k_{iipv}}/{s}\right)\left(0 - I_q\right) \quad (11)$$

Where k_{pvpv} and k_{ivpv} are the proportional and integral gains of the PV voltage loop control, and for the current loop control are k_{pipv} and k_{iipv}.

3) Battery Energy Storage System (BESS) Model

A battery device, an LCL filter, a two-level converter, and a 480V/600V transformer comprise the Battery Energy Storage System model. The BESS also has a control system shown in Fig. 11 that generates voltage reference (Vref) to the PWM generator that controls the converter output, as well as a control signal (open/close) to the grid breaker.

The battery system model is made up of 3.2V, 14Ah Lithium-ion Iron Phosphate (LFP) cells. They are grouped in many cell modules (72 modules of 4 cells) that are linked in series to make a 922V battery string. Our model's battery system consists of 80 battery strings connected in parallel to produce a system rated at 1 MWh.

The following are the primary components of the BESS control system model:

- Unit of Resynchronization

Without synchronizing the microgrid with the distribution system, out-of-phase reclosing will occur, resulting in extremely high inrush currents. To avoid this, the resynchronization device will first bring the microgrid voltage into phase with the distribution system voltage before re-closing the grid breaker. This will guarantee a smooth reconnection to the distribution system. The synchronization procedure will take 3 seconds. During that time, PI regulators will gradually bring the microgrid voltage and frequency up to par with the main grid.

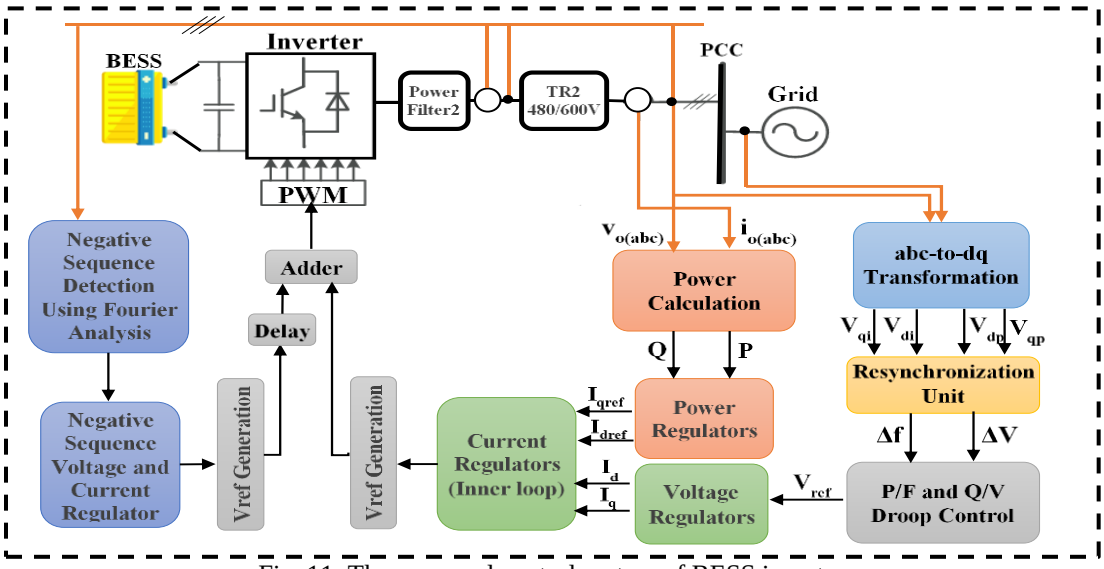

Fig. 11: The proposed control system of BESS inverter

The resynchronization block is utilized to recover the voltage deviation as well as the frequency deviation computed using PLL. These deviations will be added to the primary droop to compensate for the difference in voltage or frequency. The DC power (P_{dc}) on the DC side of the inverter and (the instantaneous active (P) and reactive (Q) powers) in dq reference frame on the AC side of the inverter are represented as [38-40],

$$P_{dc} = V_{dc} I_{dc} \quad (12)$$

$$P = \frac{3}{2}(V_d I_d + V_q I_q) \quad (13)$$

$$Q = \frac{3}{2}(V_d I_d - V_q I_q) \quad (14)$$

- Droop Control

The BESS must regulate both the frequency and voltage of the microgrid in grid-forming mode. The BESS has a droop P/F of 0.5 percent, which means that the microgrid frequency can fluctuate between 50.25 Hz (inverter absorbs its nominal active power) and 49.75 Hz (inverter produces its nominal active power). The droop Q/V is adjusted to 3%, allowing the microgrid voltage at the PCC bus to vary between 609 Vrms (inverter absorbs its full inductive power) to 582 Vrms (inverter produces its full capacitive power).

Droop control has two functions in this study: it controls real power through frequency control and controls reactive power through voltage control [41, 42].

Regulating the system's real and reactive power allows for manipulation of voltage and frequency. A droop control equation is formed as following:

The actual and reactive power in a transmission line are designed as follows:

$$P = \frac{V_1 V_2}{X} Sin\delta \quad (15)$$

$$Q = -\frac{V_1 V_2}{X} Cos\delta + \frac{V_1^2}{X} \quad (16)$$

The angle of the power (δ) is very low so $Sin\delta = \delta$ and $Cos\delta = 1$. Then equations (15) and (16) becomes,

$$\delta = \frac{PX}{V_1 V_2} \quad (17)$$

$$V_2 - V_1 \cong -\frac{XQ}{V_1} \quad (18)$$

As a result of the foregoing equations, it is evident that real power can be used to regulate the power angle. Reactive power can be used to control the voltage. Frequency control, in turn, leads to the regulation of the power angle, which controls the real power flow [43]. Finally, the microgrid's frequency and voltage amplitude are controlled by independently regulating active and reactive power. As a result, it is possible to determine the frequency and voltage droop regulation as follows [44-47]:

$$f = f_s + k_{pf}(P - P^s) \quad (19)$$

$$V = V_s + k_{QV}(Q - Q^s) \quad (20)$$

where f, V, P and Q are the measured values of frequency, voltage, active power and reactive power respectively where f_s, V_s, P^s and Q^s = the set values of frequency, voltage, active power and reactive power respectively. k_{pf}, k_{QV} = droop proportional constants.

- Power Calculation

The power calculation subsystem computes the inverter's active and reactive power. It also computes the dq components of three-phase voltages and currents at the PCC bus of the microgrid where I_d can regulate active power and I_q can control reactive power.

- Voltage and Power Regulators.

The dq voltage regulators are engaged while in grid-forming mode. They take the observed dq voltages and the reference voltage Vref and use them to calculate the reference currents I_{dref} and I_{qref}. The active and reactive power regulators use the measured power (P and Q) from the BESS primary bus (shown in Fig. 1), as well as the power reference signals Pref and Qref, to create the reference currents I_{dref} and I_{qref}.

A PI-based voltage control loop creates output dq current (I_d, I_q) signals while comparing the voltage reference

signal (V_{ref}: produced by the droop controller) with the real dq voltage components (Vd, Vq) at the input side [44].

$$I_d = \left(k_{pvb} + {k_{ivb}}/{s}\right)\left(V_{ref} - V_d\right) \quad (21)$$

$$I_q = \left(k_{pvb} + {k_{ivb}}/{s}\right)\left(0 - V_q\right) \quad (22)$$

A PI-based power control loop creates output d-q reference current (I_{dref} and I_{qref}) signals while comparing the active and reactive power with their reference values.

$$I_{dref} = \left(k_{ppb} + {k_{ipb}}/{s}\right)\left(P - P_{ref}\right) \quad (23)$$

$$I_{qref} = \left(k_{pqb} + {k_{iqb}}/{s}\right)\left(Q - Q_{ref}\right) \quad (24)$$

Where k_{pvb} and k_{ivb} are the proportional and integral gains of the BESS voltage loop control, and for the power loop control are k_{ppb} and k_{ipb}.

- Current Regulators

The Current Regulators are supplied with the I_{dref} and I_{qref} reference currents. The regulators use the measured and reference currents to generate the inverter's dq voltages (V_d and V_q). It is worth noting that the regulators accomplish high dynamical response by using feedforward computation. On the control of grid-connected inverters, current control operates as an inner loop section. Both I_d and I_q are regulated by separate PI controllers to track reference values I_{dref} and I_{qref} respectively.

The voltage references V_{drref} and V_{qrref} are created by combining the output of the PI controller with the terminal voltage in dq and the cross drop voltage in the inductor and resistor L_{ff} and R_{ff}. These voltage references control the Pulse Width Modulation (PWM), which generates the appropriate command for the grid-connected inverter's switches [44].

$$V_{drref} = \left(k_{pib} + {k_{iib}}/{s}\right)\left(I_{dref} - I_d\right) + V_d + R_{ff}I_d - \omega L_{ff}I_q \quad (25)$$

$$V_{qrref} = \left(k_{pib} + {k_{iib}}/{s}\right)\left(I_{qref} - I_q\right) + V_q + R_{ff}I_d + \omega L_{ff}I_q \quad (26)$$

Where k_{pib} and k_{iib} are the proportional and integral gains of the BESS current loop control.

- Reference Voltage Generation

V_{drref} and V_{qrref} are scaled and translated to a three-phase reference signal V_{ref}, which is sent into the PWM modulator to generate pulses for the inverter.

- Compensator for Imbalance

When imbalance compensator activated, the imbalance compensator reduces the negative sequence voltage at the PCC bus caused by grid load imbalance. It makes use of an outer-loop dq voltage regulator as well as an inner-loop dq current regulator.

4) Load

The 600V load is represented simply by a fixed three-phase load model (PQ) and a second switchable three-phase load model (PQ).

The adjusted control parameters of the adopted $\mathcal{M}$-grid are shown in Table I.

TABLE I
The adjusted control parameters.

Description	Symbol	Nominal value
Sampling time	Ts	40µsec.
Nominal frequency	Fnom	50Hz
BESS Frequency droop (%)	k_{pf}	0.5
BESS Voltage droop (%)	k_{QV}	3
BESS power regulator proportional gain	k_{ppb}	1.5
BESS power regulator integral gain	k_{ipb}	15
BESS current regulator proportional gain	k_{pib}	0.2
BESS current regulator integral gain	k_{iib}	15
BESS voltage regulator proportional gain	k_{pvb}	2
BESS voltage regulator integral gain	k_{ivb}	25
BESS PWM switching frequency	Fsw	2700Hz
Proportional gain of synchronization to distribution system	k_{psyn}	0.015/2
Integral gain of synchronization to distribution system	k_{isyn}	0.03/2
Proportional gain of PV arrays power regulator	k_{ppv}	0.05
Integral gain of PV arrays power regulator	k_{ipv}	2
PV current regulator proportional gain	k_{pvpv}	6
PV current regulator integral gain	k_{ivpv}	30
PV voltage regulator proportional gain	k_{pipv}	0.2
PV voltage regulator integral gain	k_{iipv}	15
PV PWM switching frequency	Fsw	2340Hz

5) Faults Detection and Diagnostic Using DWT

Because of its ability to resolve high-frequency components, the wavelet transform is one of the most preferred approaches for defect detection and classification. [48–51].

Ingrid Daubechies (db), a Belgian mathematician, developed the most widely used collection of discrete wavelet transformations (DWT) in 1988. The utilization of recurrence relations to create increasingly smaller discrete samplings of an implicit mother wavelet function underpins this concept.

A mathematical method for studying transitory signals is the wavelet transform. It is adopted here to detect and classify the fault type. As shown in Fig. 12, DWT is a useful tool for analyzing time-varying, transient signal-like faults by decomposing the signal into an Approximation (A) and Detailed (D) coefficients using sequential high-pass and low-pass signal filtering [52].

The noise in the fault signal can be decreased as the number of decomposition levels grows. In this study, the characteristics are extracted using a db4 mother wavelet with two layers.

By applying a signal (x) through a series of filters, the DWT is determined. After passing the samples through a low

pass filter with impulse response (g), the output is convolutional between the x and g:

$$y(n) = (x * g)(n) = \sum_{k=-\infty}^{\infty} x(k)g(n-k) \quad (27)$$

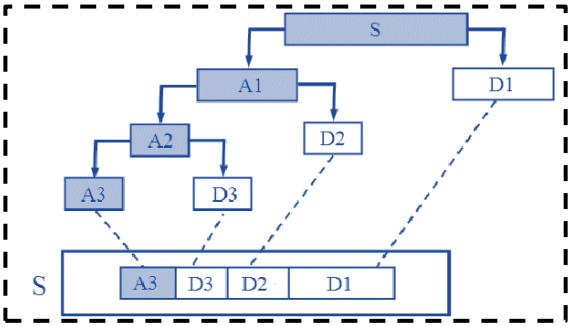

Fig.12 DWT decomposition tree

A high-pass filter (h) is used to deconstruct the signal at the same time. The detail coefficients correspond to the high-pass filter's outputs, while the approximation coefficients correspond to the low-pass filter's outputs. According to Nyquist's rule, half of the samples can now be discarded because half of the signal's frequencies have been deleted. The low-pass filter (g) output is then subsampled by 2 and further processed by running it through a new low-pass filter g and a high-pass filter (h) with half the previous one's cut-off frequency, i.e.[53]

$$y_{low}(n) = \sum_{k=-\infty}^{\infty} x(k)g(2n-k) \quad (28)$$

$$y_{high}(n) = \sum_{k=-\infty}^{\infty} x(k)h(2n-k) \quad (29)$$

Because just half of each filter output characterizes the signal, the time resolution has been decreased. The frequency resolution has been doubled since each output has half the frequency spectrum of the input.

The summation above might be expressed more succinctly.

$$y_{low} = (x * g) \downarrow 2 \quad (30)$$

$$y_{high} = (x * h) \downarrow 2 \quad (31)$$

Computing a complete convolution (x*g) with subsequent down sampling, on the other hand, would be a waste of time.

The approximation coefficients are decomposed with low pass filters and then down-sampled to boost the frequency resolution even further. This is depicted as a binary tree, with each node indicating a distinct time-frequency localization of a sub-space. A filter bank is the name given to the tree.

By adopting the wavelet transform, the threshold value is used to classify fault type in the power system. The value of the threshold is not universal and cannot be applied to all types of power systems. This threshold value will be calculated for each new power system in order to correctly categorize the various kinds of faults. Here, the threshold value is selected equal to 100 according to the maximum value of detailed phase and ground current coefficients for various faults as shown in table 1 (in result section).

The basic goal of the feature extraction is to supply significant information and maximum detail coefficients to the classifier so that it can categorize the kind of event using the computed features. The fault type is classified using the classifier block based on the threshold value.

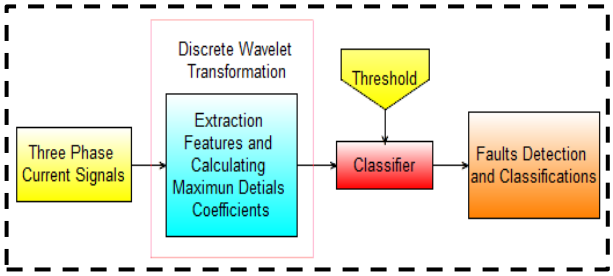

Fig.13 Faults detection and classification using DWT

The classifier classifies fault types (line to ground, double lines to ground, three lines to ground, and line to line faults) based on the values of detailed coefficients calculated by the wavelet transform for current phases A, B, and C, as well as for ground, where the classifier calculates the maximum values for these detailed coefficients and compares them to the threshold value according to table 1 of the highest detailed coefficients. Fig.14 shows the flow chart of the classification process.

Fig.14 flow chart of the classification process

III. Case Studies

The proposed microgrid model may be subjected to five case studies:

- **The first case study:**
  System operation in Grid-Following mode, PQ control, and irradiance fluctuation.
- **Second case study:**
  $\mathscr{M}$-grid transitions from grid-following to grid-forming, followed by grid resynchronization.
- **The third case study:**
  Grid-Forming mode with the power curtailment of a solar plant.
- **Fourth case study:**
  $\mathscr{M}$-grid in grid-following mode, compensating for imbalance (negative sequence).
- **Fifth case study:**
  Detecting and classification of the several fault types occurring in the location between main grid and transformer (TR4).

IV. Results And Discussion

A. The first case study shows how the adopted grid works in grid-following mode (PQ control) and how an irradiance change affects the solar plant and BESS system.

In Fig.15 and at 2 sec. the reactive power of BESS (Qbess) towards 400 kvar so that the BESS operate in capacitive mode. Because the BESS active power (Pbess)=-500kW, the BESS functions in charging mode at 4 sec. It is possible to observe the power of the PCC in brown.

Fig.16 shows how the PV irradiation drops from 500 to 100 W/m2 over time (1 sec.). This causes the solar PV power (PV voltage and current) to decrease after 1 sec. until the PV irradiation increases from 100 to 900 W/m2 at time point (3 seconds), at which point the PV power will increase.

From the Fig. 17, which indicates that the $\mathscr{M}$-grid is in grid following mode with 50Hz tracking frequency and phase shift angle near zero with PCC rms voltage around 600V. Fig.18 shows balance operation with zero negative sequence.

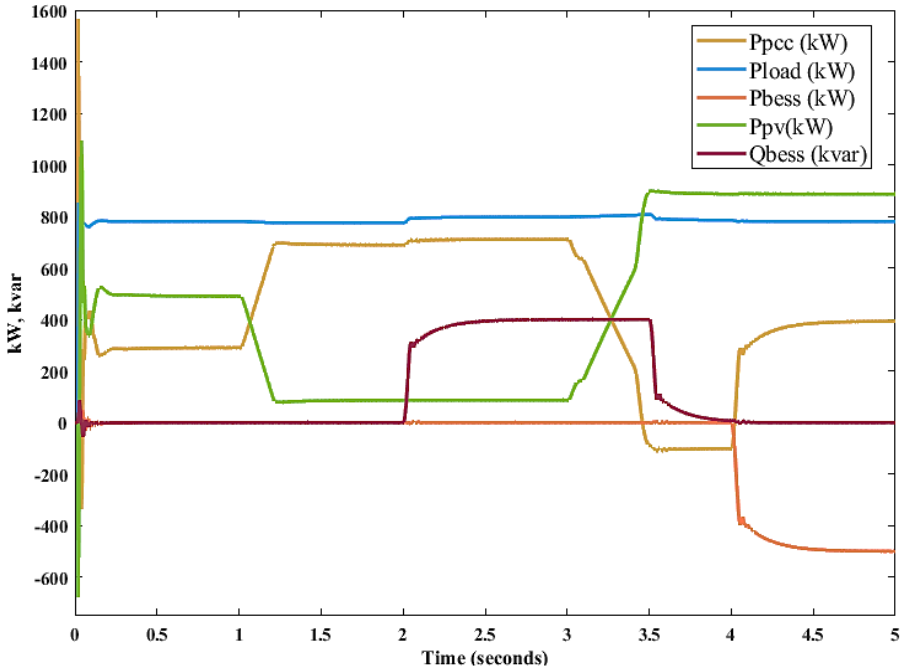

Fig.15: Load, point of common coupling, BESS, PV active power and BESS reactive power in first case

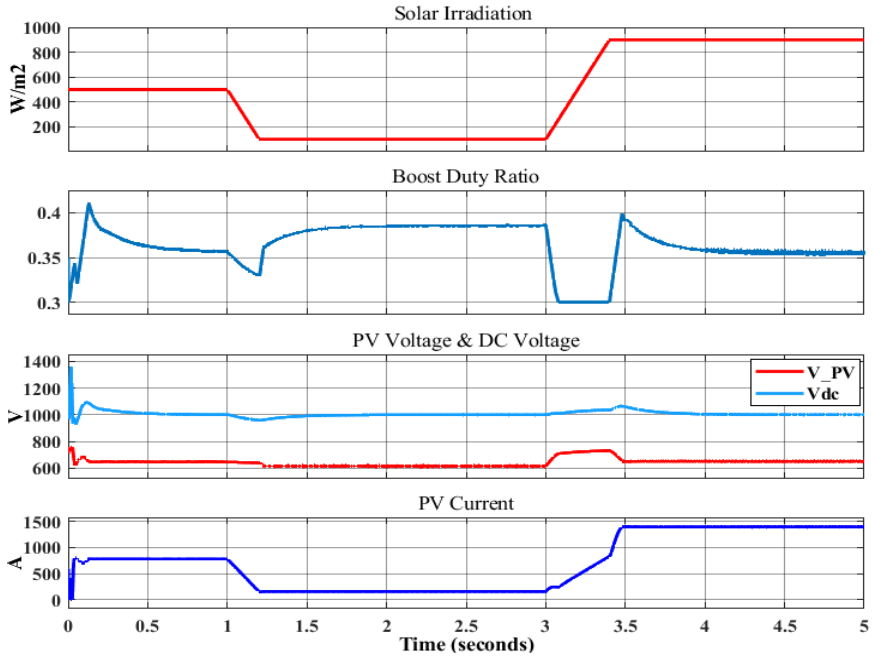

Fig.16: Solar irradiation, boost converter duty ratio, voltages of PV and converter output and PV current.

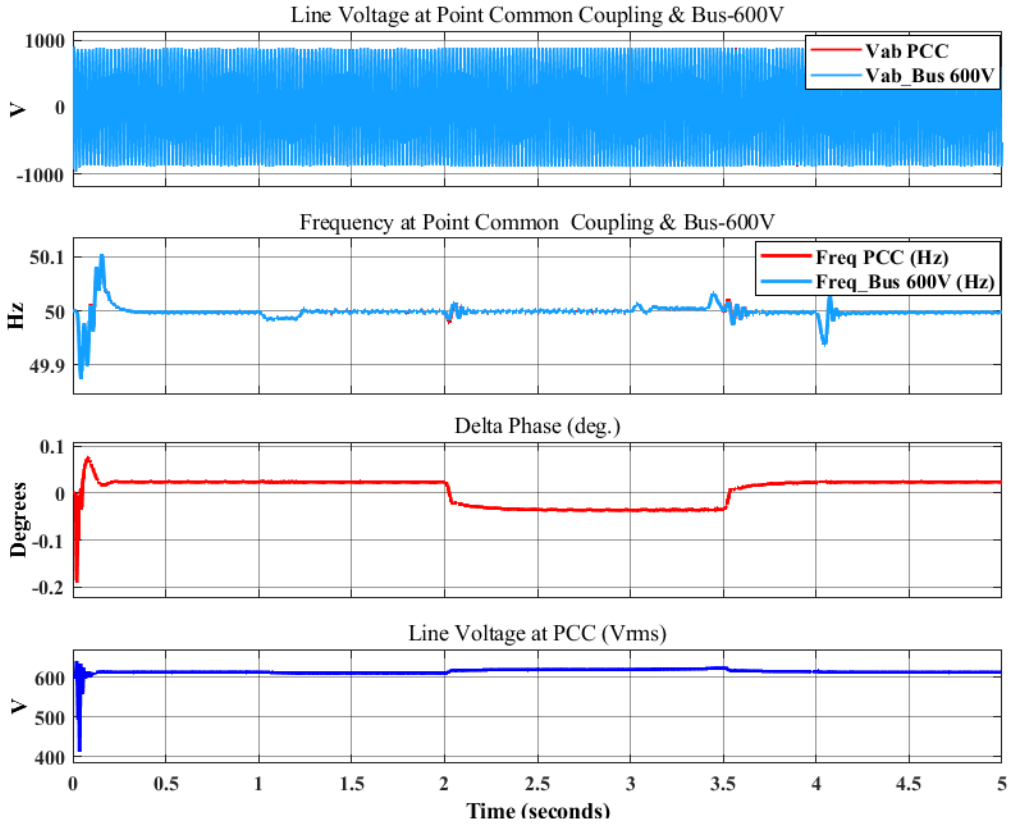

Fig.17: Voltages and frequencies of Bus-600V and PCC with phase difference in first case

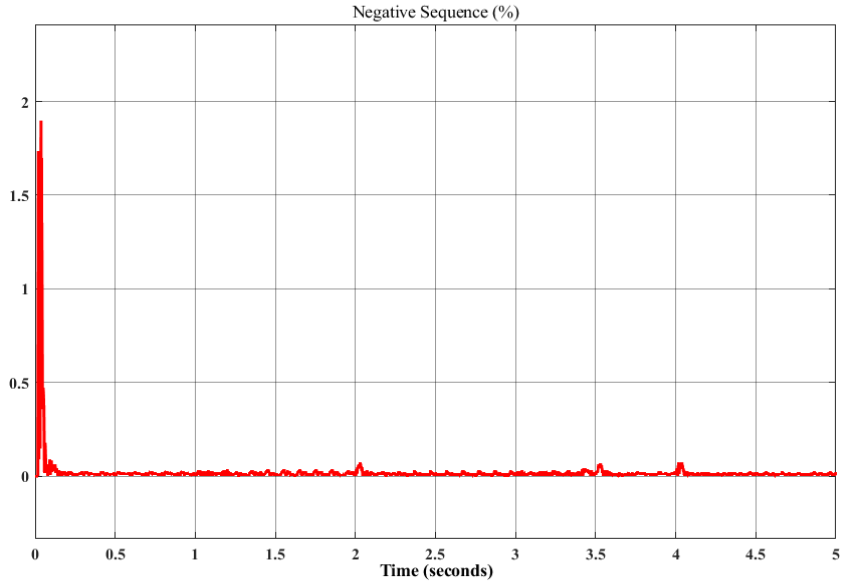

Fig.18: Percentage of negative sequence in first case.

B. In second case study, the grid-following and grid-forming are demonstrated. To reconnect the $\mathscr{M}$-grid with the distribution system, a resynchronization to the grid is undertaken. The adopted system functions in grid following mode for the first 1 second, then in islanded mode after that as shown in Figs 19-21. Figure 19 shows that the main grid power at PCC is zero ($\mathscr{M}$-grid in islanded mode) in the time interval [1-5] sec. Otherwise its operates in grid following mode.

The solar irradiation is constant at 650 W/m2 and also the boost duty ratio is near 0.35 with boost output voltage, PV voltage and current are shown in Fig.20. In Fig.21 the microgrid's frequency is kept constant at 50Hz, with a phase difference depicted in the same figure. The microgrid reconnects to the main grid at time point (9 seconds), and the frequency is exactly 50Hz, with no phase difference. Fig.22 shows the negative sequence value in the second case study.

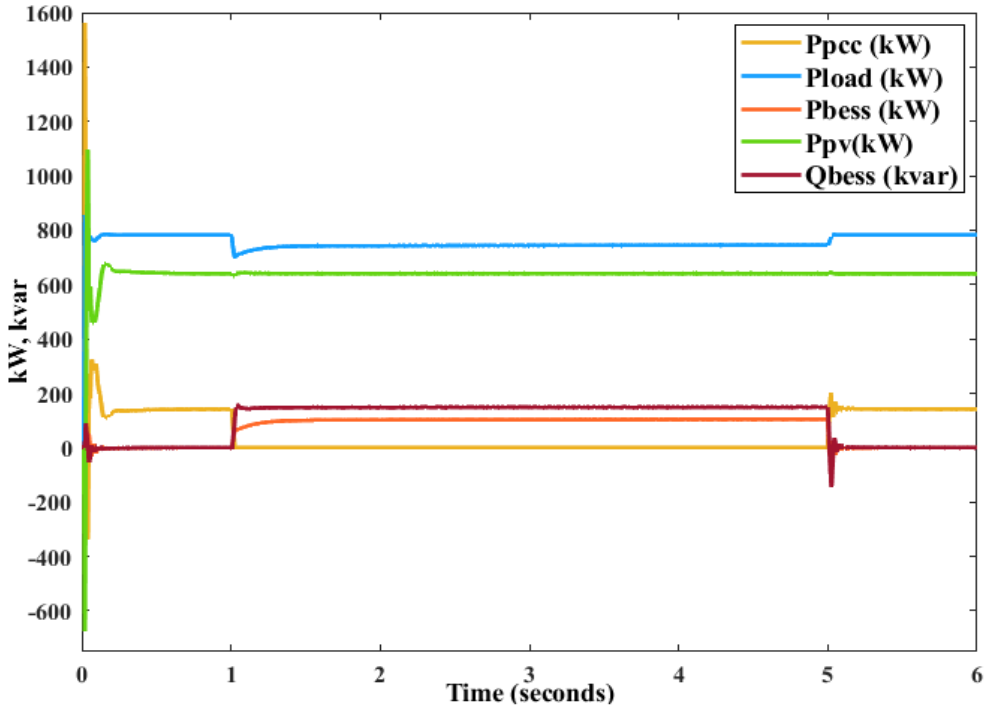

Fig.19: Load, point of common coupling, BESS, PV active power and BESS reactive power in second case.

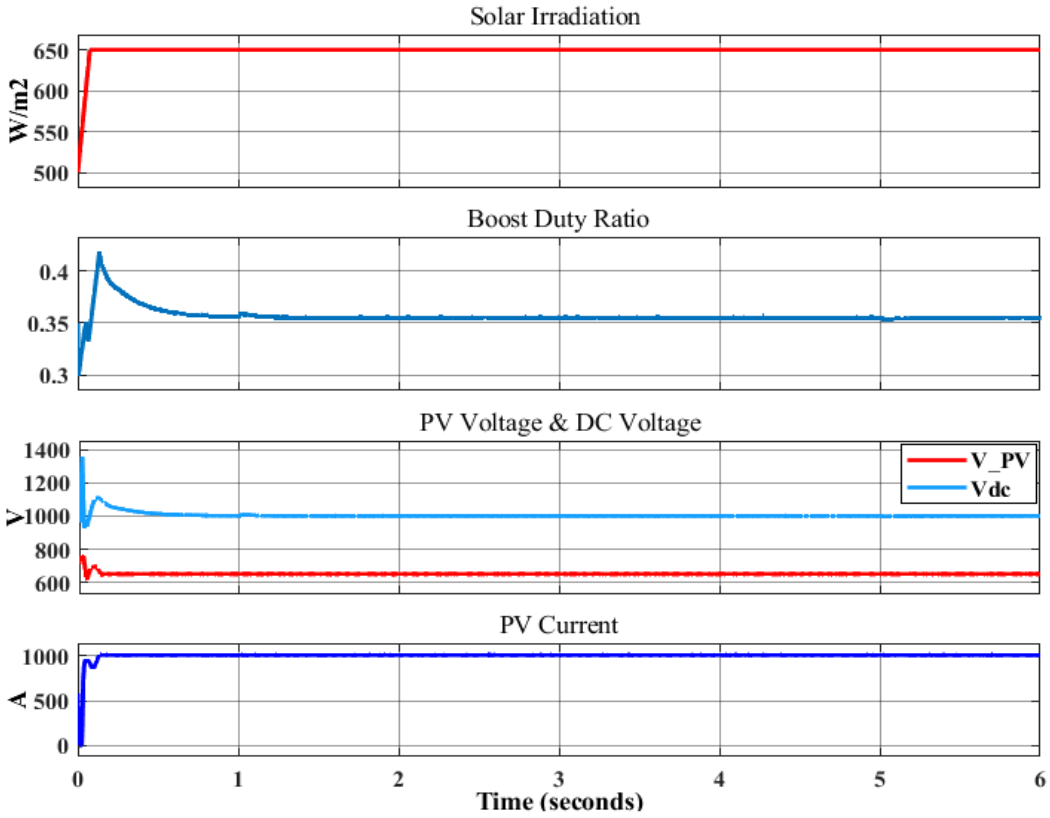

Fig.20: Solar irradiation, boost converter duty ratio, voltages of PV and converter output and PV current.

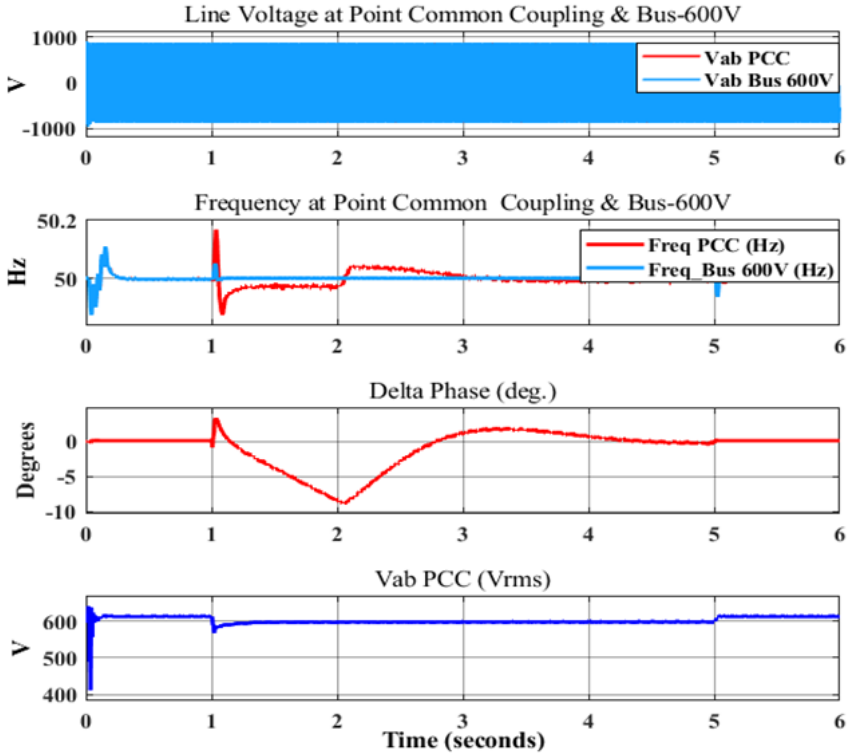

Fig.21: Voltages and frequencies of Bus-600V and PCC with phase difference in second case.

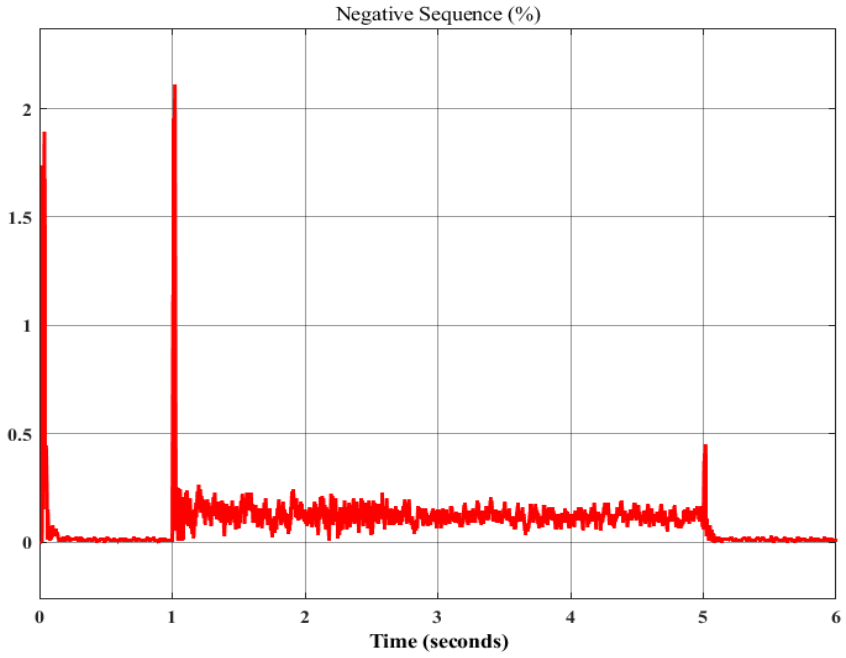

Fig.22: Zero percent of negative sequence in second case

C. Third case study reveals a curtailment in renewable energy. When considering the real solar irradiation, curtailment indicates that the PV array's production is decreased below what it could have been. A considerable load reduction is simulated in our test, resulting in a situation where the electricity generated exceeds the microgrid's load requirement (large load was turned off). The BESS then momentarily absorbs the excess power (as shown in fig.23 after 1.5 sec) and sends a signal to the PV array management system, instructing it to switch from MPPT to PQ control mode, lowering the solar plant's output power (at time point 2.5 sec.) with a reference power of 400kW. At the 1 sec., the module operates in grid following mode, then in islanded mode. Fig.24 shows solar irradiation, boost converter duty ratio, voltages of PV and converter output and PV current.

Fig.25 depicts the grid operating autonomously after time 1 sec. while preserving frequency stability at 50 with delta phase, voltage at PCC and 600V-bus. Fig.26 shows the negative sequence value in the third case study.

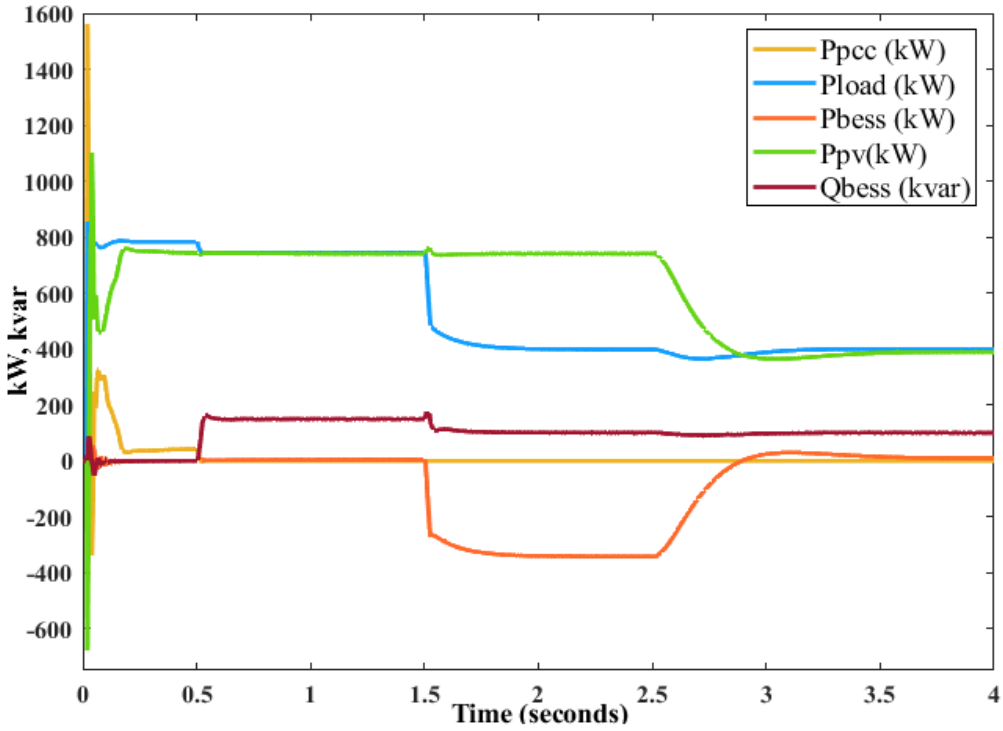

Fig.23: Load, point of common coupling, BESS, PV active power and BESS reactive power in third case study

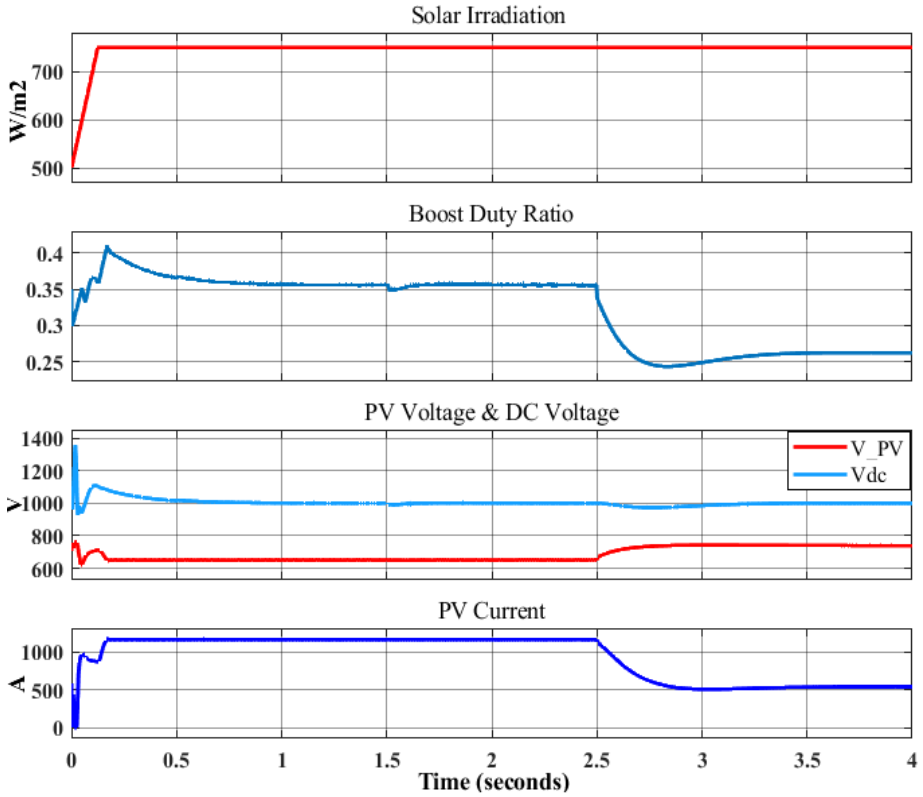

Fig.24: Solar irradiation, boost converter duty ratio, voltages of PV and converter output and PV current.

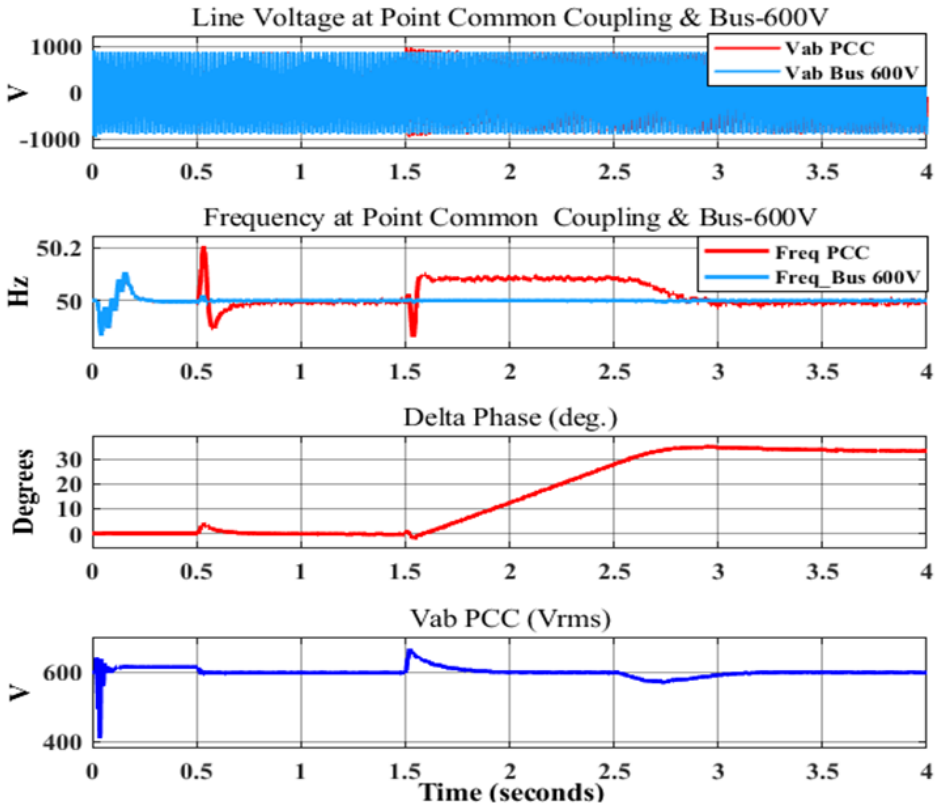

Fig.25: Voltages and frequencies of Bus-600V and PCC with phase difference in third case.

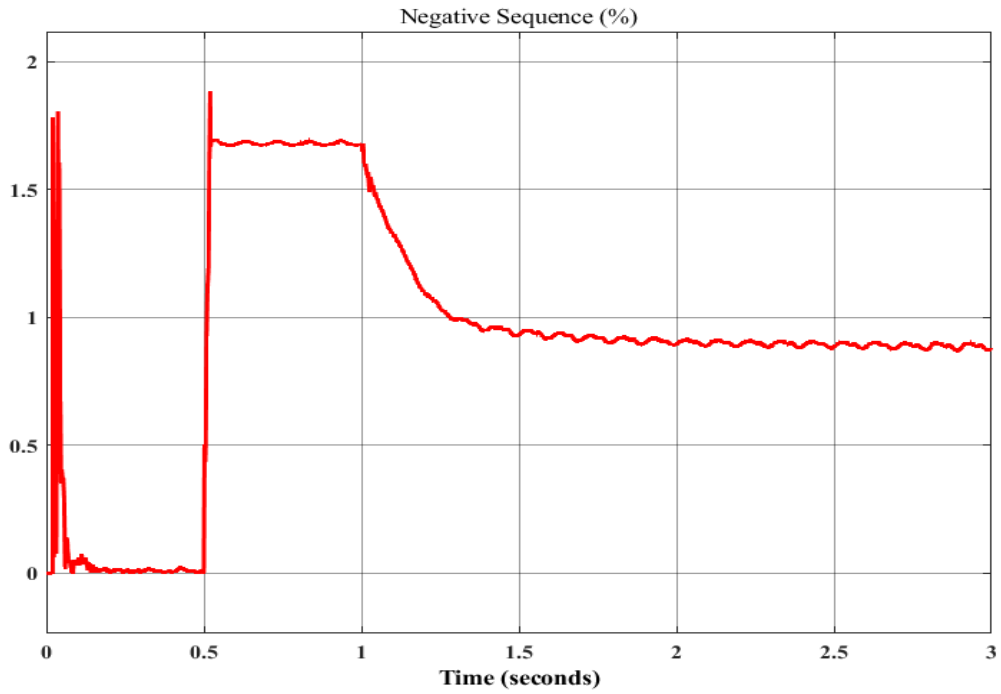

Fig.26: Zero percent of negative sequence in third case.

D. The fourth case study depicts the BESS's imbalance compensation mechanism in action. The BESS is in grid-following mode as shown in Figs. 27-29. A significant single-phase demand is turned on at 0.5s, causing a microgrid imbalance (1.5 percent negative sequence voltage). The Imbalance Compensation mechanism is enabled half a second after this event as shown in Fig. 30.

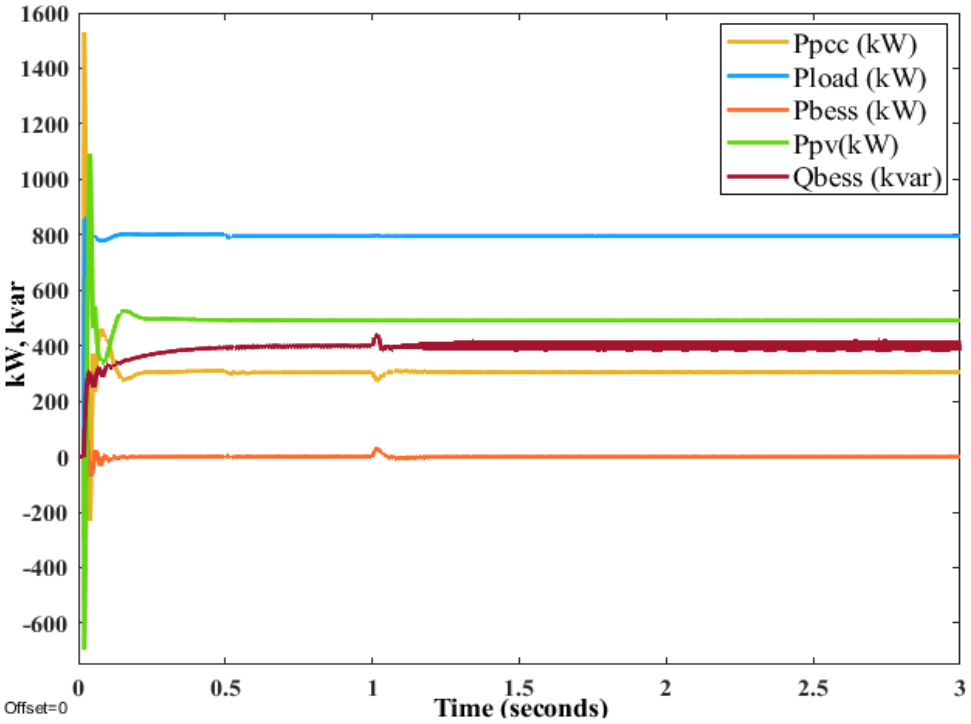

Fig.27: Load, point of common coupling, BESS, PV active power and BESS reactive power in fourth case study.

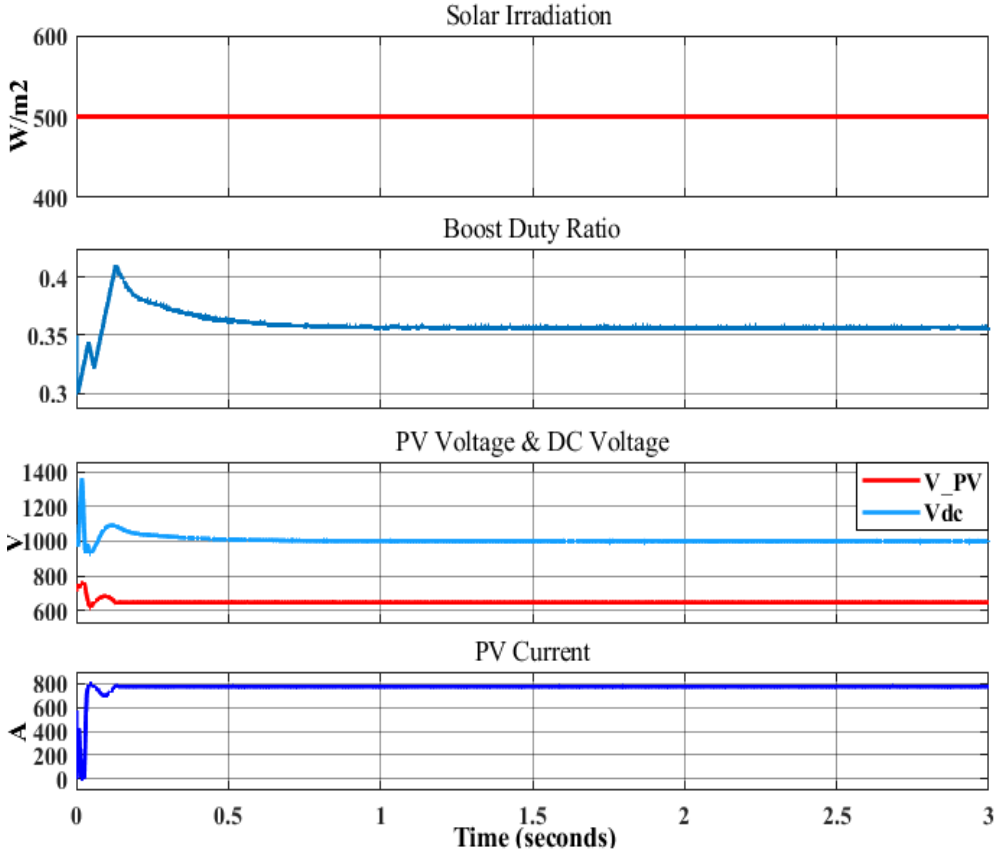

Fig.28: Solar irradiation, boost converter duty ratio, voltages of PV and converter output and PV current.

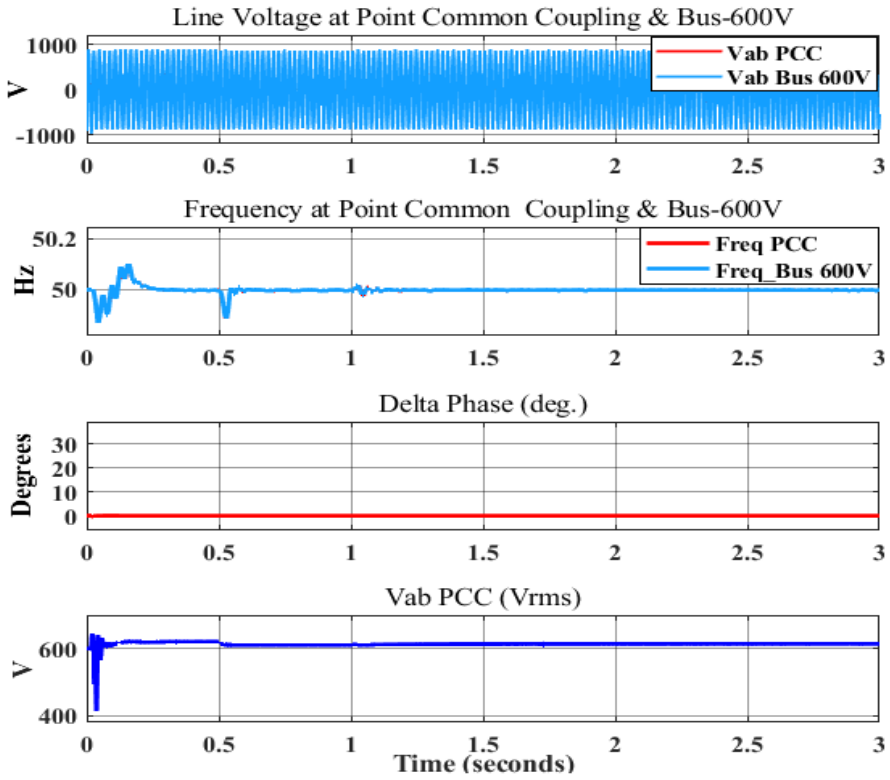

Fig.29: Voltages and frequencies of Bus-600V and PCC with phase difference in fourth case study

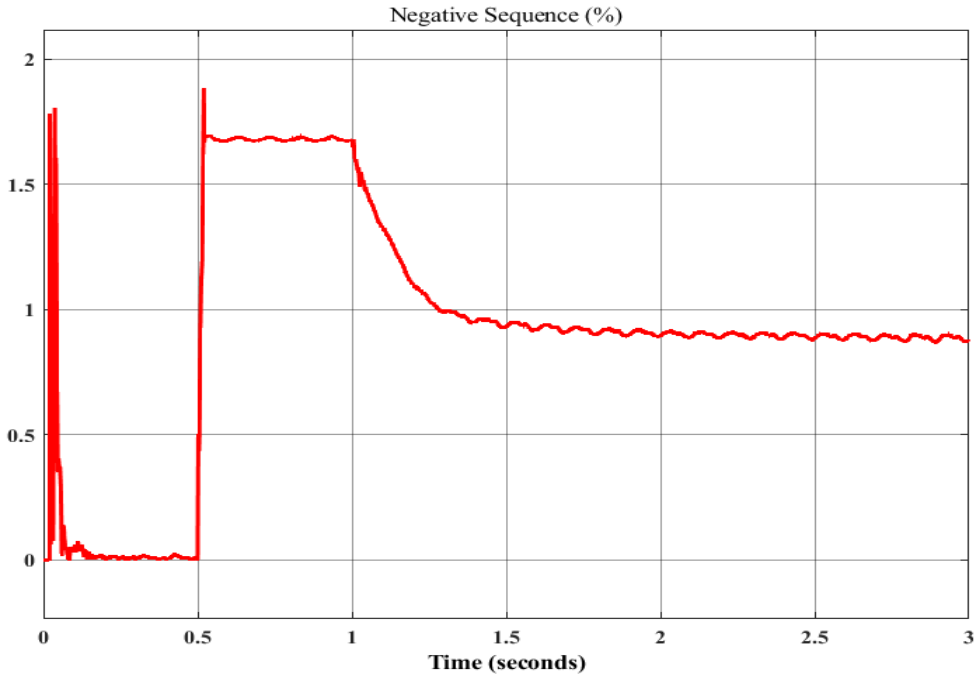

Fig.30: Percentage of negative sequence in case 4.

E. The fifth case demonstrates how to detect and diagnose the types of faults that occur in the grid, where various types of faults were produced on the location between the transformer (TR4) and the main grid, and the discrete wavelet theory was used to find and diagnose these fault. Where a three-phase fault to ground occurred at time 1 sec., a double-line fault to ground at time 2 sec., a line-to-ground fault at time 3 sec. and a line-to-line fault at time 4 sec. as shown in Figs. 31-32. The maximum values of the detailed coefficients acquired using the DWT and displayed in Table II for the adopted network are used to detect and classify faults. The value of Threshold (here it taken equal to 100) may be inferred from the table and used as a foundation for comparison and categorization.

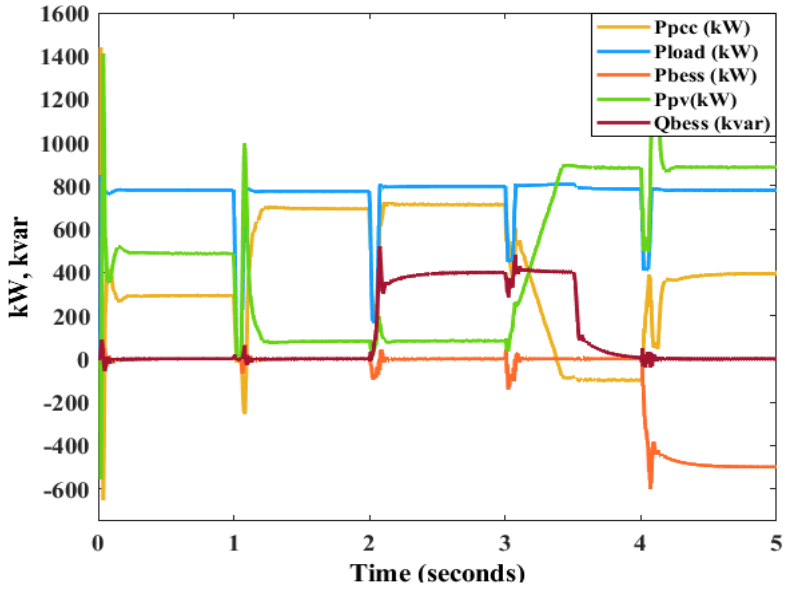

Fig.31: Load, point of common coupling, BESS, PV active power and BESS reactive power with the effects of faults.

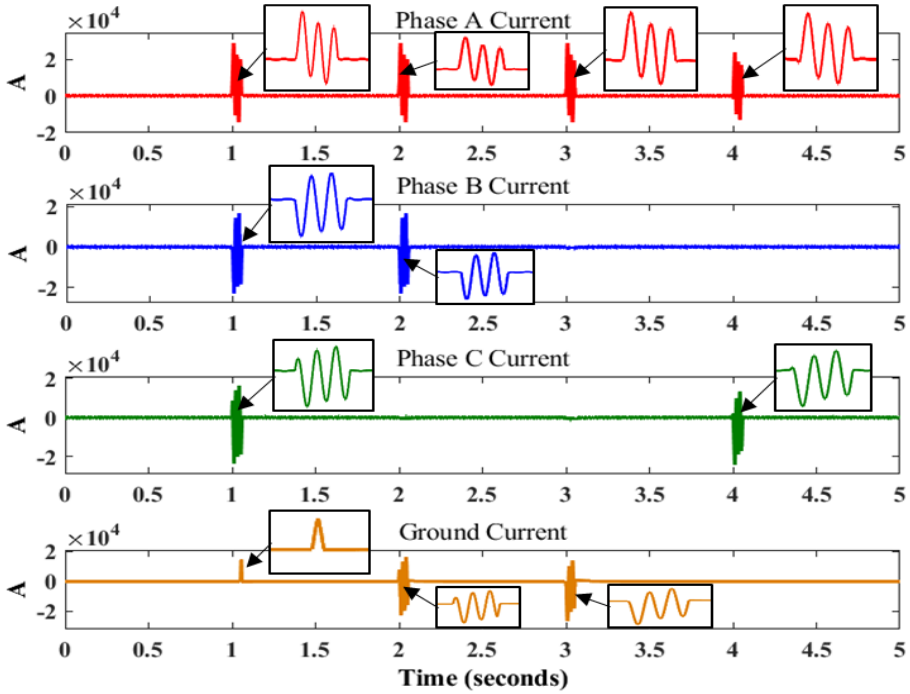

Fig.32: Different types of faults that have been done at various time points.

TABLE II

Maximum value of detailed phase and ground current coefficients for various faults.

Fault type	Phase A Current's maximum coefficient	Phase B Current's maximum coefficient	Phase C Current's maximum coefficient	Ground Current's maximum coefficient
ABC-G	**1000.923**	**2000.341**	**2000.538**	**2000.023**
AB-G	**1000.306**	**2000.34**	**92.896**	**1000.143**
A-G	**1000.304**	**40.449**	**52.796**	**1000.058**
A-C	**1000.920**	**40.456**	**2000.543**	**0.01**
N.O	**64.967**	**40.437**	**28.569**	**1.477e-11**

V. Conclusions

In this study, a suggested Microgrid made up of a PV array, BESS and three phase loads have been simulated to operate in grid following mode, autonomous mode and re-synchronization mode to seamlessly reconnect to the utility grid. Several scenarios have been operated on the proposed model to demonstrate Microgrid dynamic operation, including grid-following to grid-forming operation, followed by resynchronization to grid, solar irradiance variation, solar plant curtailment, MPPT control and PQ control. After completing multiple studies to investigate the aforementioned matters, extremely satisfying simulation results for the adopted grid were obtained, and the desired results to function in an on-grid or off-grid mode, or reconnected and resynchronized between them, were attained. Extracting the MPP using fuzzy logic, which has been shown to be successful against environmental fluctuations as well as tracking precision for maximum power. In addition, the system is capable of resolving imbalance issues due to large load introduced which causes negative sequencing. Finally, the adopted grid is able to detect and identify fault types using DWT as shown in the result subsection of case five with very accepted simulation results.

Conflict of Interest

The authors have no conflict of relevant interest to this article.

References

[1] T. Vandoorn, J. Vasquez, J. De Kooning, J. Guerrero, and L. Vandevelde, “Microgrids: Hierarchical control and an overview of the control and reserve management strategies,” IEEE Ind. Electron. Mag., vol. 7, no. 4, pp. 42–55, Dec 2013.

[2] Z.-x. Xiao and H.-w. Fang, “Impacts of P-f & Q-V droop control on microgrids transient stability,” Physics Procedia, vol. 24, pp. 276–282, 2012.

[3] S. M. Ashabani and Y. A. I. Mohamed, “A flexible control strategy for grid-connected and islanded microgrids with enhanced stability using nonlinear microgrid stabilizer, ”IEEE Transactions on Smart Grid, vol. 3, no. 3, pp. 1291–1301, 2012.

[4] C. X. Dou and B. Liu, “Transient control for micro-grid with multiple distributed generations based on hybrid system theory,”International Journal of Electrical Power and Energy Systems, vol. 42, no. 1, pp. 408–417, 2012.

[5] Wenming Guo and Longhua Mu, “Control principles of micro-source inverters used in microgrid”, Guo and Mu Protection and Control of Modern Power Systems 1:5, 2016.

[6] N. Hajilu, G.B. Gharehpetian, S.H. Hosseinian, M.R. Poursistani, and M. Kohansal, “Power Control Strategy in Islanded Microgrids Based on VF and PQ Theory Using Droop Control of Inverters”, 2015 International Congress on Electric Industry Automation (ICEIA), Shiraz, pp.37-42, 24-25 February 2015.

[7] J. Wang, M. Wang, H. Li, W. Qin, L. Wang, “Energy Management Strategy for Microgrid Including Hybrid Energy Storage”, In Proceedings of the 2018 Asian Conference on Energy, Power and Transportation Electrification, Singapore, pp. 1–6, 2018.

[8] L. Zacharia, L. Tziovani, M. Savva, L. Hadjidemetriou, E. Kyriakides, A. Bintoudi, A. Tsolakis, D. Tzovaras, J.L. Martinez-Ramos, A. Marano, et al. “Optimal Energy Management and Scheduling of a Microgrid in Grid-Connected and Islanded Modes”, In Proceedings of the 2019 International Conference on Smart Energy Systems and Technologies, pp. 1–6, 2019.

[9] Xiaoling Xiong and Yuchen Yang, “A Photovoltaic-Based DC Microgrid System: Analysis, Design and Experimental Results“, Electronics, vol. 9, no. 6, 2020.

[10] K. Rajasekhara Reddy et al, “Configurations and Control Strategy of a Single Stage Grid Connected PV System“, E3S Web of Conferences 184, 2020.

[11] Lucas O. Mogaka et al., “Islanded and Grid-Connected Control in a Microgrid with Wind-PV Hybrid”, International Journal of Applied Engineering Research, vol. 15, no. 4, pp. 352-357, 2020.

[12] Bilal Naji Alhasnawi and Basil H. Jasim, “Adaptive Energy Management System for Smart Hybrid Microgrids”, The 3rd Scientific Conference of Electrical and Electronic Engineering Researches, 2020.

[13] Bilal Naji Alhasnawi and Basil H. Jasim, “A New Coordinated Control of Hybrid Microgrids with Renewable Energy Resources Under Variable Loads and Generation Conditions”, Iraqi Journal for Electrical and Electronic Engineering, December 2020.

[14] Bilal Naji Alhasnawi and Basil H. Jasim, “A New Energy Management System of on-Grid / off-Grid Using Adaptive Neuro-Fuzzy Inference System”, Journal of Engineering Science and Technology, Vol. 15, No. 6, pp. 3903–3919, 2020.

[15] Heesang Ko et al, “Supervisory Power Coordination Scheme to Mitigate Power Curtailment in the Application of a Microgrid”, Processes 2021.

[16] K. Rayudu et al., “Design of Controller for Transition of Grid Connected Microgrid to Island Mode”, Turkish Journal of Computer and Mathematics Education, vol. 12 no.2, pp. 845-854, 2021.

[17] Nihad Abdulkhudhur Jasim and Majli Nema Hawas, “Modelling and simulation of microgrid power system including a hybrid energy storage system”, IOP Conf. Series: Materials Science and Engineering, 2021.

[18] Mehmet Emin Akdogan and Sara Ahmed, “Energy Storage System (ESS) for Compensating Unbalanced Multi-microgrids Using Modified Reverse Droop Control”, IEEE Applied Power Electronics Conference and Exposition (APEC), 2021.

[19] P. Mathiesen, M. Stadler, J. Kleissl, Z. Pecenak, “Techno-economic optimization of islanded microgrids considering intra-hour variability”, Appl. Energy, vol. 304, 2021.

[20] Mwaka I. Juma et al., “Design of a Hybrid Energy System with Energy Storage for Standalone DC Microgrid Application”, Energies, vol. 14, no. 18, 2021.

[21] S. Jamalaldin, S. Hakim and H. Razak, "Damage Identification Using Experimental Modal Analysis and Adaptive Neuro-Fuzzy Interface System (ANFIS)", Topics in Modal Analysis, Conference Proceedings of the Society for Experimental Mechanics Series 30, vol.5, pp. 399-405, 2012.
[22] K.L. Kennerud, "Analysis of Performance Degradation in CdS Solar Cells", IEEE Trans. Aerosp. Electron. Syst., AES-5, pp. 912–917, 1969.
[23] T. Easwarakhanthan, J. Bottin, I. Bouhouch, C. Boutrit, "Nonlinear Minimization Algorithm for Determining the Solar Cell Parameters with Microcomputers", Int. J. Sol. Energy, vol. 4, pp.1–12, 1986.
[24] J.A. Gow, C.D. Manning, "Development of a photovoltaic array model for use in power-electronics simulation studies" IEEE Proc. Electr. Power Appl., vol. 146, pp.193–200, 1999.
[25] J.A. Eikelboom, A.H.M.E. Reinders, "Determination of the Irradiation Dependent Efficiency of Multicrystalline Si PV Modules on Basis of IV Curve Fitting and Its Influence on the Annual Performance", Netherlands Energy Research Foundation: Petten, The Netherlands, pp. 2–5, 1997.
[26] Y. Kuo, T. Liang, J. Chen, "Novel maximum-power-point-tracking controller for photovoltaic energy conversion system", IEEE Trans. Ind. Electron, vol. 48, pp. 594–601, 2001.
[27] G. Walker, "Evaluating MPPT Converter Topologies Using a Matlab PV Model", J. Electr. Electron. Eng., vol. 21, pp. 49–55, Aust. 2001.
[28] A.H. Alqahtani, "A Simplified and Accurate Photovoltaic Module Parameters Extraction Approach using Matlab", In Proceedings of the 2012 IEEE International Symposium on Industrial Electronics, China, pp. 1748–1753, 2012.
[29] D.S.H. Chan, J.C.H. Phang, "Analytical methods for the extraction of solar-cell single- and double-diode model parameters from I-V characteristics", IEEE Trans. Electron Devices, 34, pp.286–293, 1987.
[30] V. Lo Brano, A. Orioli, G. Ciulla, A. di Gangi, "An improved five-parameter model for photovoltaic modules", Sol. Energy Mater. Sol. Cells, vol. 94, pp.1358–1370, 2010.
[31] A.K. Das, "Analytical derivation of explicit J–V model of a solar cell from physics based implicit model", Sol. Energy, vol. 86, pp. 26–30, 2012.
[32] Yao Cui et al., "A Rprop-Neural-Network-Based PV Maximum Power Point Tracking Algorithm with Short-Circuit Current Limitation", IEEE ISGT NA, 2019.
[33] Ali M.Eltamaly, "Performance of MPPT Techniques of Photovoltaic Systems Under Normal and Partial Shading Conditions ", Advances in Renewable Energies and Power Technologies, Solar and Wind Energies, Vol. 1, pp. 115-161, 2018.
[34] Sabah MIQOI et al., "Fuzzy logic PI controller for PV water pumpingsystem", International Renewable and Sustainable Energy Conference (IRSEC), 2014.
[35] D. Beriber, and A. Talha, "MPPT techniques for PV systems", 4th International Conference on Power Engineering, Energy and Electrical Drives, IEEE, Istanbul, Turkey, pp. 1437-1442, 2013.
[36] M.A. Younis, T. Khatib, M. Najeeb, and A.M., Ariffin, "An improved maximum power point tracking controller for PV systems using artificial neural network", Przeglad Elektrotechniczny, Vol. 88, No. 3, pp. 116-121, 2012.
[37] E. Lodhi, Z. Lodhi, R.N. Shafqat, and F. Chen, "Performance analysis of perturb and observe and incremental conductance MPPT algorithms for PV system", IOP Conference Series: Materials Science and Engineering, IOP Publishing, Beijing, 012029, 2017.
[38] Bilal Naji Alhasnawi, et al., "A New Robust Energy Management and Control Strategy for a Hybrid Microgrid System Based on Green Energy", Sustainability, vol. 12, 2020.
[39] Bilal Naji Alhasnawi, et al., "Distributed secondary consensus fault tolerant control method for voltage and frequency restoration and power sharing control in multi-agent microgrid", International Journal of Electrical Power and Energy Systems, vol. 133, 107251, 2021.
[40] Bilal Naji Alhasnawi and Basil H. Jasim, "A Novel Hierarchical Energy Management System Based on Optimization for Multi-Microgrid", International Journal on Electrical Engineering and Informatics, Vol. 12, No. 3, 2020.
[41] R. Majumder, B. Chaudhuri, A. Ghosh, R. Majumder, G. Ledwich, and F. Zare, "Improvement of stability and load sharing in an autonomous microgrid using supplementary droop control loop," IEEE Transactions on Power Systems, vol. 25, no. 2, pp. 796–808, 2010.
[42] F. Razavi, R. Torani, I. Askarian, A. Asgharizadeh, and N. Masoomi, "Optimal design of islanded microgrid using genetic algorithm," in International Conference on Genetic and Evolutionary Methods (GEM '12), 2012.
[43] F. Shahnia et al. "Operation and control of a hybrid microgrid containing unbalanced and nonlinear loads,"Electric Power Systems Research, vol.80, no.8, pp.954–965, 2010.
[44] Bilal Naji Alhasnawi et al., "A New Decentralized Control Strategy of Microgrids in the Internet of Energy Paradigm", Energies, vol. 14, 2021.
[45] Bilal Naji Alhasnawi et al., "A New Robust Energy Management and Control Strategy for a Hybrid Microgrid System Based on Green Energy", Sustainability, vol. 12, 2020.
[46] Bilal Naji Alhasnawi et al., "A Novel Internet of Energy Based Optimal Multi-Agent Control Scheme for Microgrid including Renewable Energy Resources", Int. J. Environ. Res. Public Health, vol. 18, 2021.
[47] Bilal Naji Alhasnawi et al., "A New Robust Control Strategy for Parallel Operated Inverters in Green Energy Applications", Energies, vol. 13, 2020.
[48] S. Devi, et al., "Detection of transmission line faults using discrete wavelet transform", In Proceedings of the 2016 Conference on Advances in Signal Processing (CASP), Pune, India; pp. 133–138, 2016.
[49] L.N. Tripathy, et al., "A differential protection scheme for tapped transmission line containing UPFC and wind farm", In Proceedings of the 2014 IEEE Students'

Technology Symposium, Kharagpur, India; pp. 319–324. 28 February–2 March 2014.
[50] A.R. Adly, et al, "Critical aspects on wavelet transforms based fault identification procedures in HV transmission line", IET Gener. Transm. Distrib, vol. 10, pp.508–517. 2016.
[51] A. Alshawawreh, "Wavelet transform for single phase fault detection in noisy environment", In Proceedings of the 2014 IEEE 8th International Power Engineering and Optimization Conference (PEOCO2014), Langkawi, Malaysia, pp. 429–434, 24–25 March 2014.
[52] Elhadi Aker et al, "Fault Detection and Classification of ShuntCompensated Transmission Line Using Discrete Wavelet Transform and Naive Bayes Classifier", Energies, vol. 13, no. 243, 2020.
[53] Prakash K. Ray, B. K. Panigrahi and P. K. Rout, "Detection of Faults in Power System Using Wavelet Transform and Independent Component Analysis", First International Conference on Advancement of Computer Communication & Electrical Technology, Murshidabad, India, October 2016.